Journal of Building Engineering 45 (2022) 103457

Contents lists available at ScienceDirect

Journal of Building Engineering

journal homepage: www.elsevier.com/locate/jobe

Test and analysis on axial performances of GFRP restraint connectors for sandwich insulation wall panels

Zhi-Zhou He [a], Peng Pan [b,*], Gen-Qi Xiao [a], Shao-Dong Shen [a], Jun-Yu Ren [a]

[a] Department of Civil Engineering, Tsinghua University, Beijing, 100084, China
[b] Key Laboratory of Civil Engineering Safety and Durability of the China Education Ministry, Beijing, 100084, China

ARTICLE INFO

Keywords:
Sandwich insulation wall panel
Restraint connector
Pull-out and push-off test
Finite element analysis
Approximate calculation formula

ABSTRACT

The sandwich insulation wall panel (SIWP) is an essential component of most building insulation systems. To achieve the satisfactory insulation effect in certain areas, such as Sweden, the thickness of insulation layer in SIWPs can reach 300 mm. However, the shear and axial compressive performances of most existing connectors at this length are unsatisfactory. The authors have previously proposed a novel GFRP connector system suitable for 60–300 mm insulation thickness, and the study on its shear behaviors has been published. This paper focuses on axial loading behaviors of the system. Three types of glass-fiber reinforced plastic (GFRP) restraint connectors, named PlateA, PlateB and Cross, were proposed. Pull-out and push-off tests were conducted to investigate their tensile and compressive failure modes. Results show that anchorage zone concrete splitting is the predominate failure mode in all pull–out tests whereas concrete punching failure is the main failure mode in push-off tests. The 300-mm-length PlateA connector and the 300&150-mm-length PlateB connectors buckled before concrete failure. The concrete failure surface was determined, and formulas to calculate axial strength of connectors based on concrete failure modes were established by theoretical and finite element analysis.

1. Introduction

Sandwich insulation wall panels (SIWPs) have been widely adopted in building insulation systems due to their superior fire-resistance, durability, heat insulation and structural performance [1]. SIWP consists of two concrete layers and a middle insulation layer. The three layers are linked by a system of connectors. The outer layer is subjected to the gravity, wind loads as well as seismic loads, and the inner layer is fixed to the structure. Thus, the connector system is used to transfer the tension, compression, shear and the consequent bending moment to the inner layer and the structure [2].

Mechanical performances of various connectors have been extensively studied over the past decades. Research of single connectors mainly focuses on their tensile, compressive and shear behaviors. Huang [3] and Tomlinson [4] proposed a 50-mm-length hexagonal-tube-shaped GFRP connector and a 60-mm-length BFRP-steel connector, respectively, and tested their shear behaviors. Porter [5] proposed a 51-mm-length pin connector and measured the compressive strength. The main failure mode was found to be concrete punching failure. Xue [6] designed a 150-mm-length GFRP flat connector and proposed the formula to estimate the pull-out strength, but the accuracy of the formula was not satisfactory. Some research studies focus on SIWP's overall behaviors rather than individual connectors. Joseph [7] studied the overall in-plane shear behavior of the SIWP with 50 and 100-mm-length truss connectors. The shear performance is determined by the shear strength of connectors, shear strength of the insulation, and bonding shear strength between the insulation and concrete. Hodicky [8] found that the 150-mm-length CFRP grid connectors buckled when the SIWP is under compression. Other researches were related to different cross-section shapes of connectors, materials of insulation layer and etc [9–13]. It is worth noting that connector lengths in most studies are less than 150 mm. However, Imbabi [14] found that 300 mm insulation thickness is required for a satisfactory insulation effect in certain countries such as Sweden. The increase in connector length can affect its shear and compressive performances. When the insulation thickness reaches 300 mm, shear stiffness of most connectors does not meet the design requirements and some axially loaded components will buckle prematurely.

There are two typical types of connector systems in SIWPs. The system of grid/truss connectors has a relatively high degree of composite action, i.e., the degree of continuity between the outer and inner layers [15]. The system of discrete connectors usually has little or no composite

* Corresponding author.
E-mail address: panpeng@mail.tsinghua.edu.cn (P. Pan).

https://doi.org/10.1016/j.jobe.2021.103457
Received 21 January 2021; Received in revised form 26 September 2021; Accepted 12 October 2021
Available online 14 October 2021

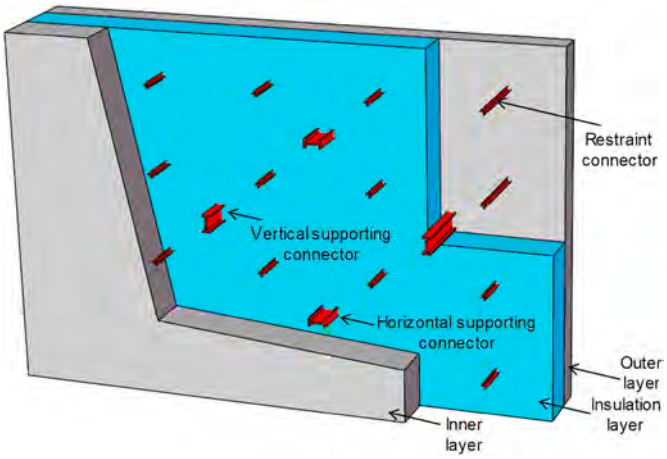

Fig. 1. Discrete connector system.

action, which makes the SIWP easier to design. There are two worldwide commercial discrete connector systems, Halfen® [16] and Thermomass® [17]. Halfen® connector is made of metal with relatively high thermal conductivity that compromise the wall's insulation efficiency [15,16]. Thermomass® system adopted a single type of uniformly arranged connector in SIWPs to simplify the design process [17]. Excessive number of connectors need to be deployed in Thermomass systems to satisfy the shear demand, which caused a large safety margin in axial direction and thus decreased its economic viability.

To address the issues mentioned above, the authors [18] has proposed a new discrete connector system designed for 60–300 mm insulation thickness SIWPs, as shown in Fig. 1. The system is comprised of GFRP supporting connectors and restraint connectors. Supporting connectors have a relatively large cross-section, featuring high shear stiffness and strength, to transfer in–plane shear loads, caused by gravity, in-plane seismic action, and overall temperature change [19]. Restraint connectors have a relatively small cross-section and are utilized to resist out-of-plane axial loads, caused by wind action, out-of-plane seismic action and temperature gradient [19]. Two types of connectors can be employed to resist external actions in a cooperative manner and such system is structurally more effective than Thermomass®.

The authors carried out a series of experiments to verify the design and mechanical properties of connectors. Shear failure modes of supporting connectors in 60–300 mm lengths have been studied, and the strength and stiffness estimation formulas were proposed [18]. This paper focuses on the connectors subjected to axial load. Three types of restraint connectors with different cross-section shapes were proposed with experiments conducted to investigate their individual properties. Axial pull-out and push-off tests were conducted to evaluate the tensile and compressive failure modes, strength and the influence factors for each connector. Through theoretical and finite element analysis, the formulas of connector strength based on anchorage zone concrete failure were established. The discrepancies between calculation and test results were identified and discussed.

2. Connector designs

In the discrete connector system, restraint connectors are evenly arranged on wall panels to transfer out-of-plane loads and restrain the deformation of the outer layer. Low shear stiffness is an important characteristic of restraint connectors to allow thermal expansion and contraction of inner and outer layers. If restraint connectors have high shear stiffness, it will cause the large internal stress in the outer layer, even result in cracks. Fig. 2 shows three types of proposed connectors. The "PlateA" and "PlateB" connectors have a rectangular cross-section. These two types of connectors are designed to investigate the influence of the cross-section size on the axial performance of the connectors. The "Cross" connector has a cross-shaped cross-section, and its cross-section area is smaller than that of "PlateA" and "PlateB" connectors. The cross-section shape enables the "Cross" connector to have the similar mechanical properties in two orthogonal directions. The experimental results of the "Cross" connector and two "Plate" connectors were compared to investigate the influence of cross-sectional shape on axial mechanical properties.

The proposed connectors adopted groove ends to provide reliable anchorage to wall panels. That is, several triangular grooves are situated at each end of the connector, as indicated by dashed line in Fig. 2. The PlateA and PlateB connectors have two grooves at each end, and the Cross connector has four grooves at each end. Fig. 3 shows the typical anchorage arrangement of a connector. The anchorage is achieved through embedded regions at connector's ends, and the embedded depth is 50 mm at each end. The load is transferred to concrete through the contact between concrete and the side surface of the groove when subjected to axial load. There is no adhesive layer between concrete and

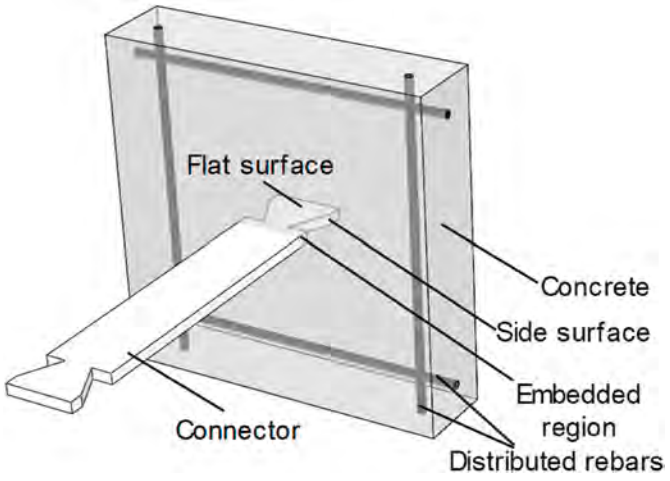

Fig. 3. Anchorage arrangement of connectors.

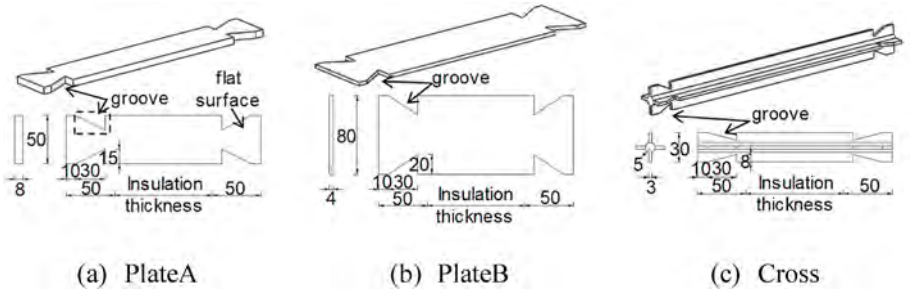

Fig. 2. Three types of novel GFRP restraint connectors.

Table 1
Material properties of GFRP.

Material property	Value	Standard deviation	Test method
longitudinal tensile strengthX_t	1114.3 MPa	30.4 MPa	ISO 527–4:1997
transverse tensile strengthY_t	55.4 MPa	1.9 MPa	
longitudinal modulus of elasticityE_1	48.5 GPa	2.8 GPa	
transverse modulus of elasticityE_2	12.6 GPa	0.6 GPa	
Poisson's ratio ν_{12}	0.27	0.02	
longitudinal compressive strengthX_c	453.9 MPa	17.5 MPa	ISO 604:2002
transverse compressive strengthY_c	123.4 MPa	5.0 MPa	
in–plane shear strength$S$	37.3 MPa	2.2 MPa	ISO 14129-1997
in–plane shear modulus of elasticityG_{12}	6.7 GPa	0.5 GPa	

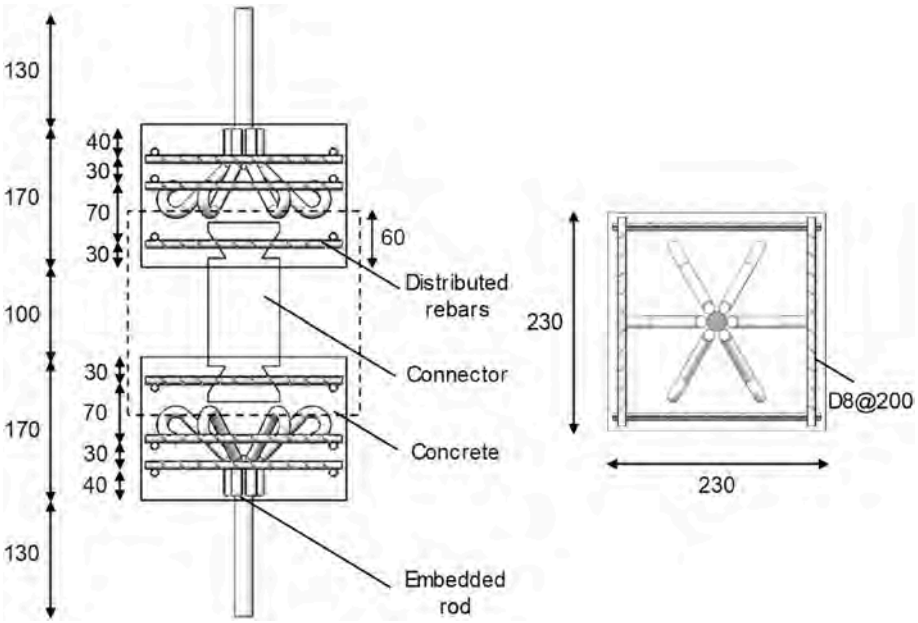

Fig. 4. Dimension of pull-out test specimens (in mm).

the flat surface of the connector. In the subsequent tests of this paper, the connectors were all anchored as described above.

Fiber reinforced polymer (FRP) has been widely used for connectors due to its high tensile strength, high corrosion resistance and low thermal conductivity. The proposed connectors were made from GFRP with the matrix of epoxy resin. The volume fraction of fiber in connectors was about 60%. For the PlateA and PlateB connectors, most fibers were aligned along the length of the connector to provide high axial tensile strength. Some ±45° multiaxial fiber cloths were added in connectors to enhance its shear strength, the content of which accounts for about 25%

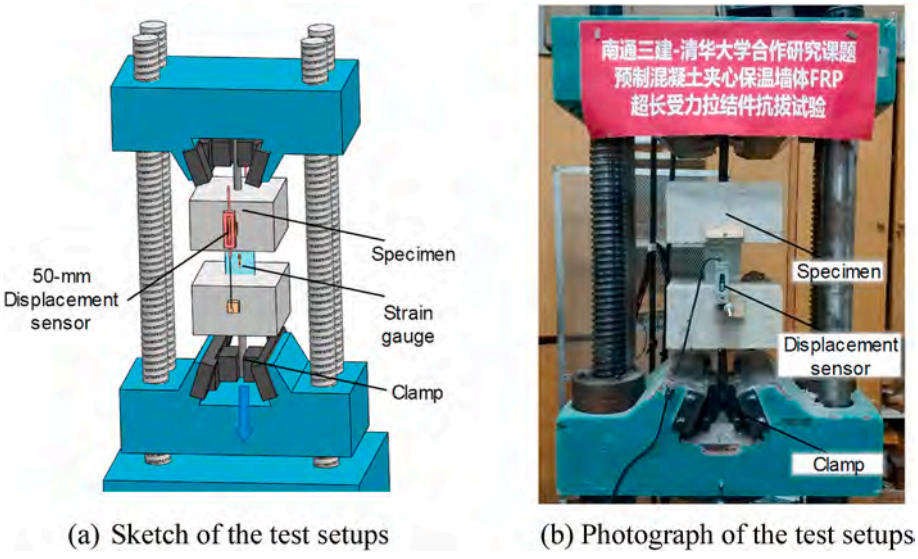

Fig. 5. Pull-out test and measurement setups.

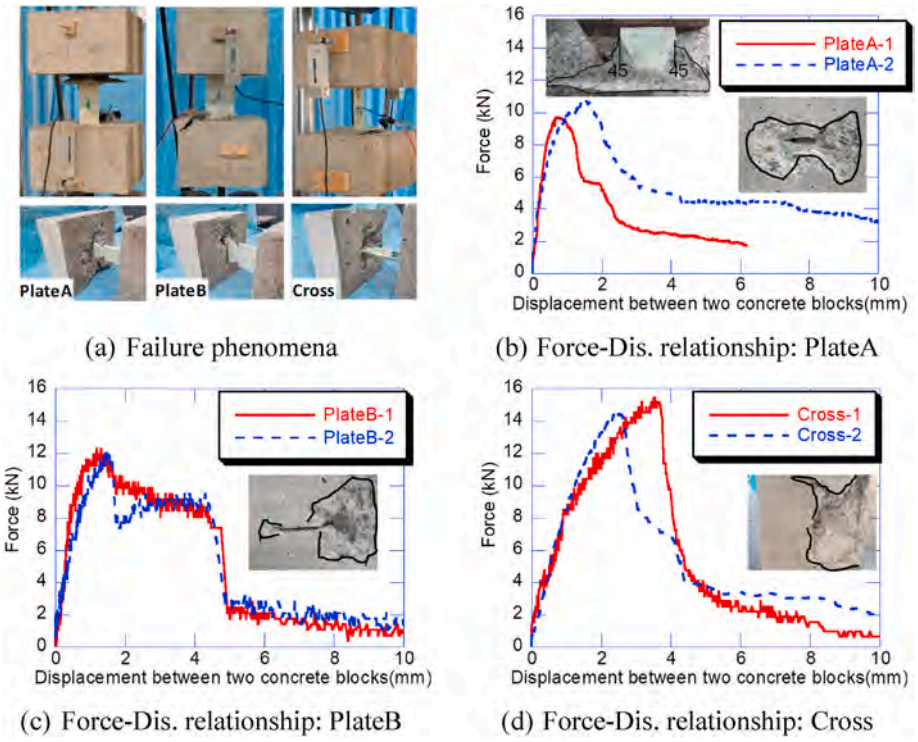

Fig. 6. Failure phenomena and force–displacement relationships.

of the total fiber. For the Cross connector, all fibers are arranged uni-directionally and along the length of the connector. These connectors were manufactured through pultrusion process with post–treatment, i.e., cutting out the grooves. The mechanical properties of GFRP lamina were tested according to the respective ISO standards [20–22]. Three identical specimens were prepared for each connector. Table 1 presents the values and standard deviation of each material property, including longitudinal tensile strength X_t, longitudinal modulus of elasticity E_1, the Poisson's ratio ν_{12}, transverse tensile strength Y_t, transverse modulus of elasticity E_2, longitudinal compressive strength X_c, transverse compressive strength Y_c, in-plane shear strength S and in-plane shear modulus of elasticity G_{12}.

3. Pull-out test

3.1. Design of pull-out test specimen

Pull-out tests were carried out to investigate the tensile failure modes and anchorage strength of the connectors outlined above. Two identical specimens were prepared for each type of connector to reduce the effects of random errors, and there are 6 specimens in total. Each batch of specimens were carried out under a relatively consistent and stable temperature, so the influence of temperature change on test results is negligible. Fig. 4 shows the detailed dimensions of PlateA specimens. Two 230mm × 230mm × 170 mm concrete blocks were connected by a restraint connector. To apply the tension load, two steel rods were embedded in concrete. Three layers of rebar were set in each block. The first layer of rebar was used to simulate the distributed rebar in SIWPs. The specimen partially highlighted by the dashed line was designed to simulate the outer layer of SIWPs with a typical thickness of 60 mm. The other two layers of rebar were used to avoid the embedded rod from being pulled-out. The connector length, or the equivalent of insulation thickness, was fixed to 100 mm as it does not affect its tensile strength. The insulation layer was not included in experiments because it has little effect on transferring tensile load. The 28-day cubic compressive strength of concrete was 34.0 MPa with the standard deviation of 1.0 MPa. The yield and ultimate tensile strength of steel were 359 MPa and 451 MPa with the standard deviation of 7.1 MPa and 9.0 MPa, respectively.

3.2. Test setup and measurement scheme

Fig. 5 shows the pull-out test setups. Two steel rods were gripped by a pair of clamps. The upper clamp was fixed, and the lower clamp can move downward to exert the tension load. The monotonic load was applied, because the number of cycles of temperate change has little effect on connector's mechanical behavior [16,19]. The load was applied with displacement-control at a rate of 0.2 mm/min. The built-in force sensor was used to measure the reaction force. Two displacement sensors were placed on the front and rear sides of the specimen to measure the relative displacement between two concrete blocks. Two strain gauges were attached along the axis on the front and rear sides of

Table 2
Pull-out test results.

Specimen ID	Peak load P_f (kN)		Peak strain $\varepsilon(\times 10^2\mu\varepsilon)$		Displacement at peak load u(mm)	
	Individual	Average	Individual	Average	Individual	Average
PlateA-1	9.6	10.2	4.1	5.0	0.7	1.2
PlateA-2	10.8		5.9		1.6	
PlateB-1	12.3	12.1	10.4	10.1	1.2	1.3
PlateB-2	11.9		9.8		1.4	
Cross-1	15.5	15.1	17.7	16.4	3.5	3.0
Cross-2	14.7		15.0		2.4	

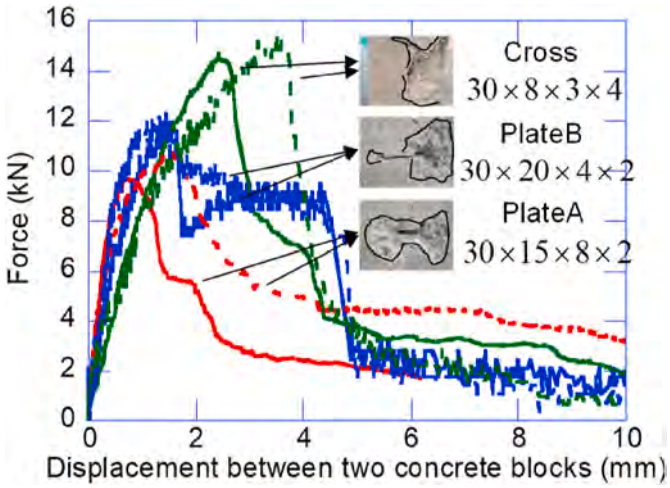

Fig. 7. Comparison among three types of connectors.

the connector to measure the axial strain.

3.3. Pull-out test results

Fig. 6(a) shows the typical failure phenomena of PlateA, PlateB and Cross connectors, respectively. Anchorage failure indicated by concrete cracking and connector pull–out can be observed in all specimens. At the peak load, a narrow crack developed on the surface of the concrete. As the displacement further increased, the crack widened. The failure surface was gradually formed and the connector was pulled out. No obvious damage was observed on connectors. Fig. 6(b), (c) and 6(d) show the force-displacement relationships of each type of specimens, respectively. The displacement is taken as the average value recorded by two displacement sensors. The slopes of the curves in Fig. 6(b)–(d) remained virtually unchanged until about half of the peak load. After that, the slope slightly decreased until the load peaked, indicating that certain damage occurred in concrete of anchorage region. After the peak, the load sharply decreased. The concrete cone attached to the connector after the pull-out process is shown in Fig. 6(b), and the double-cone failure surface can be observed. The cone surface developed outward at an angle of about 45° until it reached the outer surface of the concrete block. In the test, the bonding strength between FRP and concrete is neglectable because the surface of the FRP connector is smooth, thus the pull-out strength was mainly contributed by the contact between the connector and the concrete within the groove. This can be verified by the shape of the concrete failure surface, as shown in Fig. 6 (b)–(d). Table 2 shows the peak load, strain and the corresponding displacement of each specimen. The maximum axial strain of the connector is considerably smaller than the rupture strain of GFRP.

Fig. 7 compares the force-displacement relationships of three connectors. The dimensions of each connector's groove are listed in terms of height × width × thickness × number of grooves, which can be seen in

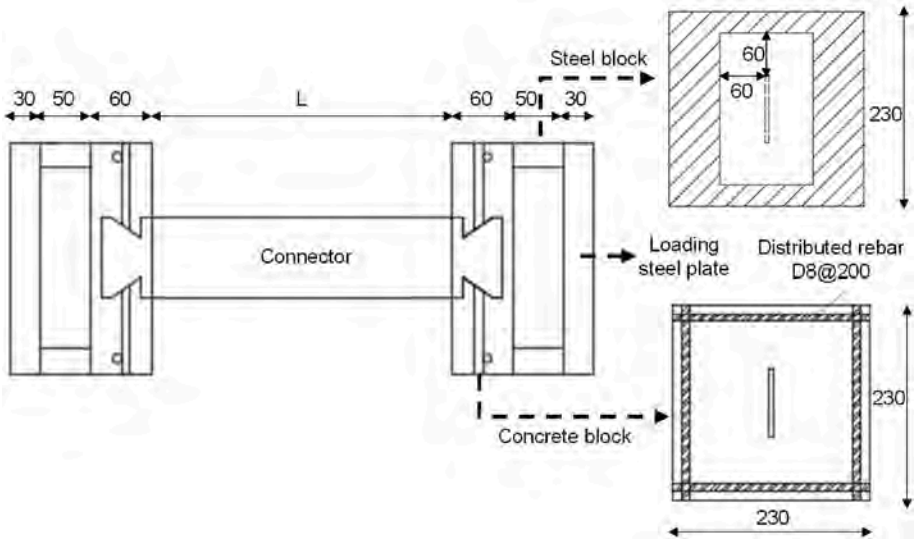

Fig. 8. Layout of push-off test specimens (in mm).

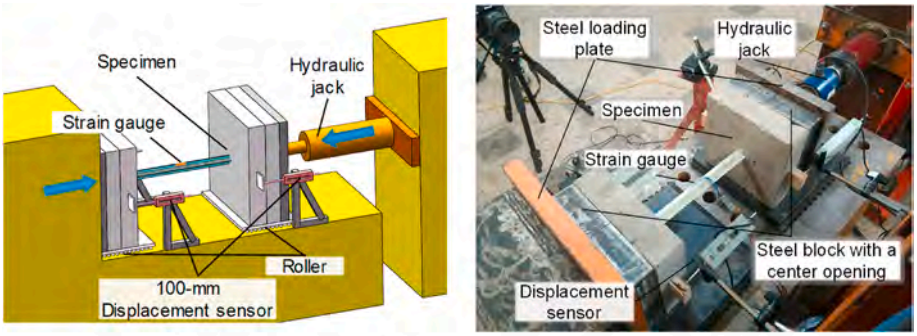

Fig. 9. Push-off test and measurement setups.

Table 3
Push-off test results.

Specimen ID	Failure mode	Peak load P_f (kN)		Strain $\varepsilon(\times 10^2\mu\varepsilon)$		Displacement u(mm)		Specimen ID	Failure mode	Peak load P_f (kN)
		Individual	Average	Individual	Average	Individual	Average			Individual
PlateA–CT300-1	Buckling	19.0	18.7	6.3/-22.6	5.9/-20.9	4.4	4.7	PlateB–CT300-1	Buckling	6.1
PlateA–CT300-2	Buckling	18.3		5.4/-19.1		5.0		PlateB–CT300-2	Buckling	4.7
PlateA–CT150-1	Punching	22.5	23.0	−10.6	−10.3	4.9	4.5	PlateB–CT150-1	Buckling	21.2
PlateA–CT150-2	Punching	23.4		−10.0		4.1		PlateB–CT150-2	Punching	27.3
PlateA–CT120-1	Punching	24.4	24.5	−10.2	−10.3	3.0	4.3	PlateB–CT120-1	Punching	22.3
PlateA–CT120-2	Punching	24.6		−10.4		5.6		PlateB–CT120-2	Punching	24.8
PlateA–CT60-1	Punching	24.8	24.2	–	–	4.4	4.3	PlateB–CT60-1	P + B	35.3
PlateA–CT60-2	Punching	23.5		–		4.1		PlateB–CT60-2	Punching	27.2

Fig. 2. The initial slope of the PlateA and PlateB connectors are slightly steeper than that of the Cross connector. This is because the slope of the curve in the elastic range represents the axial stiffness of the connector. The axial stiffness is directly proportional to the cross-sectional area, according to the formula of axial stiffness [23]. The cross-sectional area of the PlateA (400 mm^2) and PlateB connectors (320 mm^2) are much larger than that of the Cross connector (201 mm^2). The failure surface of PlateA specimens was relatively symmetrical, while the failure surfaces of PlateB and Cross specimens were not. The possible explanation is that the PlateB and Cross connectors have a relatively smaller groove thickness and resulting smaller contact area with concrete. Therefore, the PlateB and Cross connectors are more sensitive to imperfections of the concrete mixture, such as cavity and large aggregate sizes (of 10 mm grain size and above). The deviations in the mechanical performance of grooves created uneven stress distribution and resulted in asymmetric failure surface.

The average pull-out strength of the PlateA, PlateB and Cross connectors were 10.2, 12.1 and 15.1 kN, respectively. The Cross connector had the highest pull-out strength because it had four grooves at each end, which exhibited a higher overall anchorage effect than the other connectors with two grooves. The pull-out strength of the PlateB connector was higher than that of the PlateA connector. The reason was that the PlateB connector had a larger groove area (30 mm × 20 mm) than the PlateA connector (30 mm × 15 mm), which provided a better anchorage effect with each groove.

4. Push-off test

4.1. Design of push-off test specimen

To study the failure modes and measure the compressive strength of the restraint connectors, a series of push-off tests were conducted. The failure modes of three types of connectors, each with four different lengths were investigated. Two identical specimens were prepared for each type of connector with different lengths to reduce the effects of random errors, and there are a total of 24 specimens. All specimens were named in the form of X-CT-L-1/2, where X referred to the restraint connector type (PlateA, PlateB and Cross), CT referred to the compressive test, and L referred to the thickness of the insulation layer (60, 120, 150 and 300 mm).

Fig. 8 shows the layout of push-off test specimens. Two 230 mm × 230 mm × 60 mm concrete blocks, simulating the outer layers in SIWPs, were connected by a restraint connector. The connector was anchored as described in section 2. The typical thickness of the outer layer of SIWPs in engineering practices is 60 mm. Four 8-mm-diameter steel rebar were set in each concrete block to simulate the distributed rebar of SIWPs. L represented the distance of two concrete blocks, i.e., the insulation thickness. In order to apply the compressive force and allow the punching shear of concrete, a steel block with a center opening was placed between the concrete block and the loading plate. The distance between the inner edge of the opening and that of the connector was 60 mm, which is higher than the anchorage depth of the groove. The insulation layer was neglected in specimens. The reason was that the insulation foam has limited impact on the compression response of panels due to its low stiffness comparing to other components. Besides, the mechanical properties of connectors are the focus of the experiments. In addition, the effect of the insulation layer on preventing the buckling and twist of the connectors is neglected in tests since it is sensitive to imperfections in construction. Moreover, the absence of insulation layer in test design provides reasonable safety margin for engineering applications. The mechanical properties of concrete and steel were the same as those in pull-out tests.

4.2. Test setup and measurement scheme

Fig. 9 illustrates the push-off test setup. One end of the hydraulic jack was fixed on the reaction frame, and the other end moved to apply uniform compressive load on the specimen through the steel loading plate. The loading process is displacement-controlled at a rate of 0.5 mm/min. A set of rollers were placed between the specimen and the bearing to reduce friction. The built-in force sensor was used to record the reaction force. Four displacement sensors, divided into two sets, were installed to measure the relative displacement between two concrete blocks. Two strain gauges were attached at the middle of the connector to measure its axial strain. For the specimens with the insulation thickness of 60 mm, strain gauges were not installed because of space restraint. Fig. 9(b) shows a photograph of the actual push-off test environment.

4.3. Push-off test results

Table 3 gives the failure modes, peak load, axial strain and corresponding displacement of each specimen. Figs. 10–12 show the failure phenomena of each connector. Fig. 10 shows the test results of PlateA connectors of different lengths. The displacement in the figure is the average of measured value of two sets of displacement sensors. For PlateA-CT300 specimens, a sudden out-of-plane buckling of the connector occurred at the peak load of 18.7 kN, resulting in the twist of the concrete block and a sudden drop of the reaction force. The buckling capacity calculated according to the Euler stability formula $P = \frac{\pi^2 EI}{(\mu l)^2}$ was 23.2 kN, where E, I, μ and l represent the longitudinal modulus of elasticity, cross–section moment of inertia about the weak axis, effective length factor, and thickness of insulation layer, respectively [23]. In the tests, the concrete block at one end is fixed and the other end is pinned, so the corresponding effective length factor is 0.7 [23]. It is worth noting that the outer layer in the actual panel may not produce such a twist because of other restraint. Such boundary conditions are used in tests for the convenience of loading. Experimental results were slightly smaller than theoretical Euler stability capacity, which can be due to the eccentricity of the specimen under loading. At the peak load, the axial strains on the front and rear sides of the middle of the connector were

Peak load P_f (kN)	Strain $\varepsilon(\times 10^2\mu\varepsilon)$		Displacement u(mm)		Specimen ID	Failure mode	Peak load P_f (kN)		Strain $\varepsilon(\times 10^2\mu\varepsilon)$		Displacement u(mm)	
Average	Individual	Average	Individual	Average			Individual	Average	Individual	Average	Individual	Average
5.4	13.0/-16.4	15.0/-18.4	8.8	7.2	Cross–CT300-1	Punching	21.9	23.1	−22.5	−23.0	5.1	5.2
	17.0/-20.3		5.5		Cross–CT300-2	Punching	24.2		−23.5		5.2	
24.2	−8.8/-15.0	–	3.8	3.8	Cross–CT150-1	Punching	20.6	20.9	−25.5	−24.9	5.6	6.9
	−15.8		3.7		Cross–CT150-2	Punching	21.2		−24.3		8.2	
23.6	−14.1	−15.0	4.3	4.5	Cross–CT120-1	Punching	27.4	26.8	−22.4	−22.8	3.8	3.8
	−15.9		4.7		Cross–CT120-2	Punching	26.1		−23.2		3.8	
31.3	–	–	7.9	6.6	Cross–CT60-1	Punching	20.5	22.6	–	–	3.0	4.0
	–		5.2		Cross–CT60-2	Punching	24.7		–		5.0	

$5.9 \times 10^2\mu\varepsilon$ and $-\ 20.9 \times\ 10^2\mu\varepsilon$, respectively. Twist of the concrete block and buckling of the connector further developed as the displacement was increased, while the reaction force remained mostly unchanged. PlateA-CT150, PlateA-CT120 and PlateA-CT60 specimens had the similar failure phenomena, i.e., concrete punching failure, because their buckling loads are larger than punching shear capacities. Concrete damage mainly occurred surrounding the connector's groove. The failure surface expanded from the inner concrete, i.e., the original location of the groove, to the outer surface of concrete blocks. The average punching capacity of these specimens was about 23.9 kN. The average axial strain at the peak load was about $-\ 10.3 \times 10^2\mu\varepsilon$, which is much lower than the compressive failure strain of GFRP material. With the increase in the loading displacement, the connector gradually penetrated concrete, and the reaction force decreased.

Fig. 11 shows the push-off test results of the PlateB connectors with four different lengths. Buckling occurred in the PlateB-CT300-1&2 and PlateB-CT150-1 specimens. The average peak load was 5.4 kN and 21.2 kN, and the buckling capacity calculated by Euler stability formula was 4.6 kN and 18.5 kN, respectively. Experimental results were slightly larger than the theoretical Euler stability capacity. The possible reason is that the end is not completely pinned due to the friction. Out-of-plane bending occurred at the mid-span of the connector when the peak load is reached. At the peak load, the average axial strains at mid-span on each side of the PlateB-CT300 specimens were $15.0\times 10^2\mu\varepsilon$ and $-\ 18.4 \times 10^2\mu\varepsilon$, respectively. The axial strains at mid-span on each side of the PlateB-CT150-1 specimen were $-8.8 \times 10^2\mu\varepsilon$ and $-\ 15.0 \times\ 10^2\mu\varepsilon$. PlateB-CT150-2, PlateB-CT120-1&2 and PlateB-CT60-2 specimens exhibited concrete punching failure. The average punching capacity was 25.4 kN and the axial strain was about $-\ 15.3 \times 10^2\mu\varepsilon$. However, the PlateB–CT60–1 specimen exhibited concrete punching and connector buckling almost simultaneously. At the load of about 27 kN, punching failure occurred. With the increase in the loading displacement, the connector gradually twisted and buckled, which led to the uplift of the concrete block at the loading end. A possible reason was that after punching failure, an eccentric load was developed which makes the connector prone to buckling. In addition, two sets of identical specimens, i.e., PlateB-CT150-1&2 and PlateB-CT60-1&2, exhibited different failure modes. It can be caused by the potential imperfections in specimen fabrication and loading process.

Fig. 12 shows the failure phenomena and force-displacement relationships of the Cross connectors with four different lengths. Punching shear failure was observed in all specimens. The average punching load was 23.4 kN whereas the Euler buckling capacity for the 300 mm length connector was 76.5 kN. There is a correlation between the distribution of the depth of the failure surface and the location of the groove. For the failure surface in the plane where the groove of the connector was located (area 1), the concrete fracture surface gradually extended outwards from the base of the grooves. The initial angle of the failure surface was less than 45°. As the failure surface extended outward, the angle gradually increased to more than 45°, until it reached the outer surface of the concrete block. The angle between the vertical axis and the dash line as shown in Fig. 12 was about 45°. The other region of failure surface (area 2) was relatively shallow, i.e., there was relatively less concrete brought out during the punching process of the connector. A possible explanation was that in terms of the force transmission path, the force mainly concentrated along the plane where the groove was located, hence the concrete failure surface in area 1 was deeper.

The failure mode of Cross connectors is consistent throughout the experiment. That is, when the connector length ranges between 60 mm and 300 mm, only concrete punching failure occurred. However, the failure modes of the other two connectors gradually change from anchorage concrete punching to connector buckling, as the connector length increases. Therefore, the Cross connector is ideal for SIWPs with thick insulation layers because of its consistent mechanical properties.

5. FEA and failure surface identification

Test results indicate that the failure mode of most pull-out and push-off specimens is concrete anchorage failure. It is necessary to propose the estimated formulas of the axial strength of the connector based on concrete anchorage failure mode, for facilitating the optimization and design of connectors for engineering practices in the future. To determine the stress distribution of concrete in the anchorage region as well as the shape and location of the failure surface, FEA models were established to simulate and analysis the results. By observing the stress nephograms, the inner crack development can be obtained.

5.1. FEA model

A three-dimensional FE model was established in the general FE analysis software ABAQUS. Fig. 13(a) shows its overall view. The dimensions of the components in the FE model are consistent with the push-off test. The Cross connector is selected for FE analysis. Because the cross section is a biaxially symmetric section, when subjected to axial force, it is assumed that each of the four webs of the cross bear the load independently and according to the superposition principle, it can be regarded as a combination of two plate connectors in the orthogonal direction [23].

In the FE model, eight-node hexahedral solid elements (C3D8R) are adopted to simulate the connector and concrete block, and the element size was selected as 2 mm based on a convergence study that will be discussed in detail in section 5.2. Truss elements (T3D2) of 20 mm size were used to simulate the rebar. A cavity is created in the concrete block where the connector is inserted. To simulate the contact between concrete and the connector, surface-to-surface contact is used. The groove surface and the concrete inner surface in contact with groove are selected as the slave and master surface, respectively. The normal behavior of the contact is "hard" contact [24]. The tangential behavior of the contact includes a penalty friction formulation with a friction coefficient of 0.6, which is a common friction coefficient between concrete and GFRP [25]. Bonding effect is not considered in the FE model since the bonding strength between FRP and concrete is negligible,

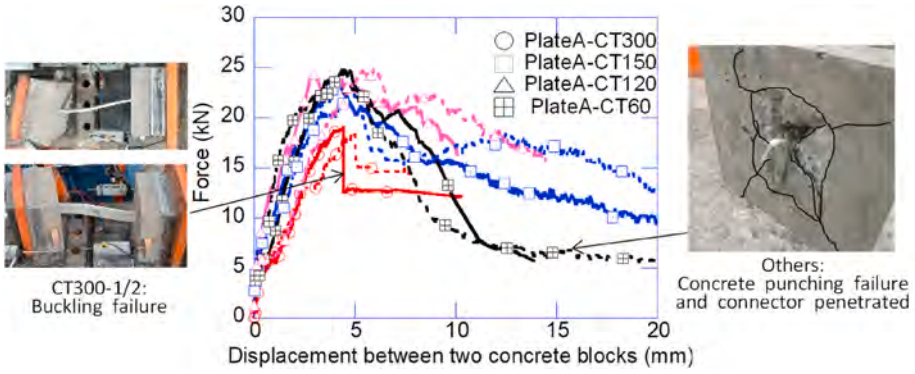

Fig. 10. Push-off test results of PlateA connectors.

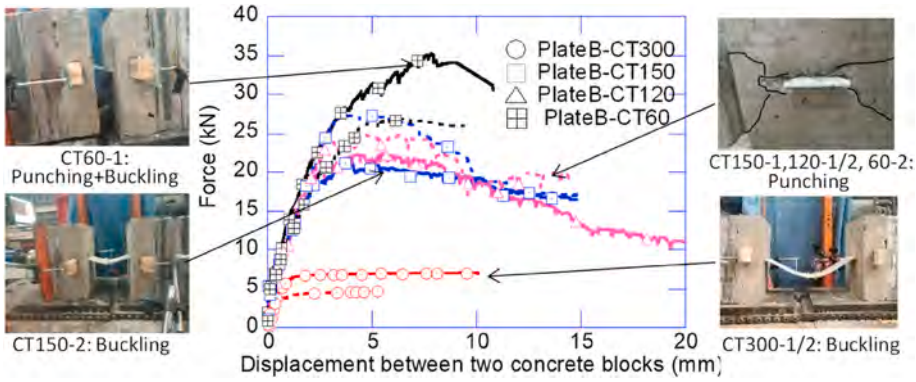

Fig. 11. Push-off test results of PlateB connectors.

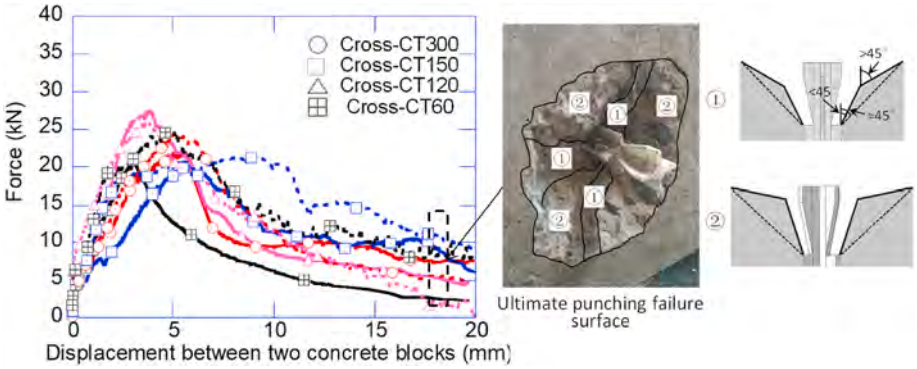

Fig. 12. Push-off test results of Cross connectors.

which was confirmed by experimental phenomena. Translational degrees of freedom around the concrete block are constrained to simulate the boundary conditions of concrete. The rebar is implanted in the concrete by "embedded" technique in ABAQUS.

In terms of the material properties and failure criteria, isotropic material and homogenous section are used to define concrete, with the Young's modulus of 30 GPa and Poisson's ratio of 0.2 [26]. The concrete damaged plasticity (CDP) model is adopted to simulate the failure of concrete [24]. Tables 4 and 5 exhibit the main parameters and relationships among the stress, strain and damage index of concrete in CDP model, which are determined according to material property tests and the code [26]. The "lamina" material type is used to define the elastic behavior of GFRP, the parameters of which are determined by previous test values. The Hashin damage model is adopted to simulate the failure criteria of GFRP [27], and Table 4 shows its main parameters. The values of fracture energy are obtained from Pinho [28]. These data are feasible because the expected main failure mode is not FRP failure, thus the FEA results are not sensitive to these values. The steel rebar is simulated as an isotropic material with Young's modulus of 200 GPa and Poisson's ratio of 0.3, and the bilinear model is intended for defining the mechanical properties.

A compression load is applied on the end surface of the connector, following a displacement-controlled pattern. A static and general analysis step is adopted, and the geometrical nonlinearity is enabled by turning on the "nonlinear geometry" option.

5.2. FEA results

A convergence study is first conducted to ensure the feasibility of the model. The mesh size of concrete to be tested are 2.5 mm, 2 mm and 1.5 mm. Fig. 14 shows the force-displacement relationships of Cross-CT150-1 test and FE results of different mesh sizes. Results show that 1.5 mm

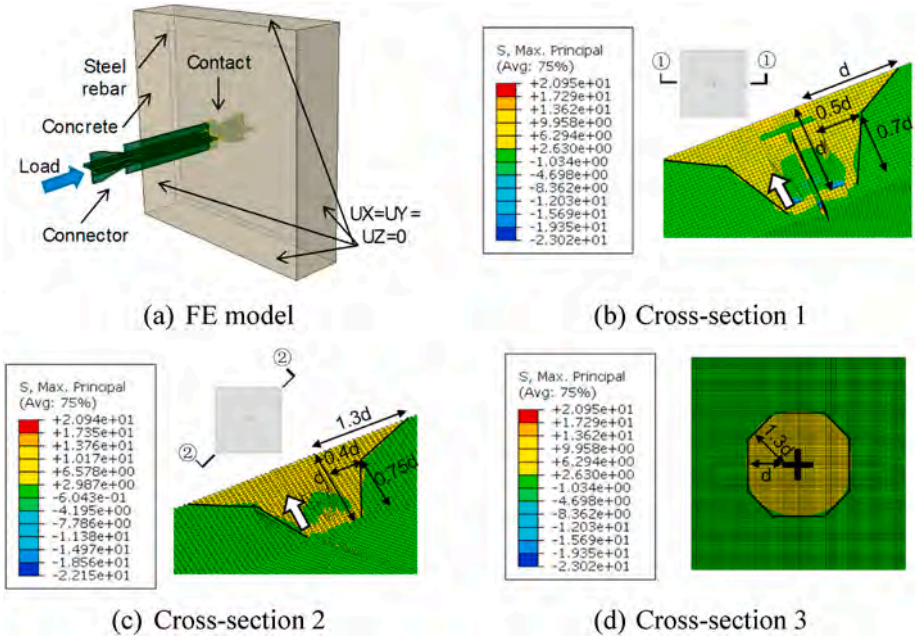

Fig. 13. FEM verification.

Table 4
Material properties in FE models.

Concrete	Value	Determination method	GFRP	Value	Determination method
Dilation Angle	36.31	Numerical fitting	E_1	48.5 GPa	Material property tests
Eccentricity	0.1		E_2	12.6 GPa	
fb0/fc0	1.16		ν_{12}	0.27	
K	0.6667		$G_{12} = G_{13} = G_{23}$	6.7 GPa	
Viscosity Parameter	0		Longitudinal tensile strength	1114.3 MPa	
Compressive yield stress	22.7 MPa	Material property tests	Longitudinal compressive strength	453.9 MPa	
Tensile yield stress	2.19 MPa		Transverse tensile strength	55.4 MPa	
			Transverse compressive strength	123.4 MPa	
Steel	**Value**	**Determination method**	Longitudinal/Transverse shear strength	37.3 MPa	
Yield stress	359 MPa	Material property tests	Longitudinal Tensile Fracture Energy	91.6 kJ/m^2	Obtained from [26]
Ultimate stress	451 MPa		Longitudinal Compressive Fracture Energy	79.9 kJ/m^2	
Ultimate plastic strain	0.1		Transverse Tensile Fracture Energy	0.2 kJ/m^2	
			Transverse Compressive Fracture Energy	1.0 kJ/m^2	

Table 5
Relationships among stress, strain and damage index in CDP model.

Compressive stress (MPa)	Inelastic strain	Damage index	Tensile stress (MPa)	Crack strain	Damage index
16.080	0.000000	0.000	2.190	0.000000	0.000
20.074	0.000185	0.100	0.988	0.000069	0.172
21.922	0.000367	0.167	0.891	0.000093	0.239
22.614	0.000558	0.229	0.771	0.000122	0.323
21.407	0.001106	0.383	0.674	0.000150	0.399
18.267	0.001631	0.517	0.524	0.000209	0.544
14.171	0.002358	0.666	0.434	0.000264	0.645
9.257	0.003661	0.826	0.371	0.000320	0.721
4.053	0.007505	0.957	0.269	0.000479	0.842
2.273	0.012424	0.985	0.227	0.000594	0.887
1.922	0.014436	0.989	0.133	0.001219	0.965

mesh size gives the similar results with those of 2 mm mesh, but requires nearly 4.3 times the calculation time (CPU time 65 h vs. 15 h). Therefore, the concrete mesh size is chosen as 2 mm.

The qualitative analysis is adopted here to investigate the shape of concrete failure surface by drawing the maximum principal stress nephograms of concrete on different cross-sections. The locations of cracks were obtained through observing the distribution of the maximum principal stress.

Fig. 13(b)–(d) show the maximum principal stress nephograms of concrete elements in three cross-sections. The elements highlighted in yellow exhibit a relatively high value of maximum principal stress and that concrete failure occurred in these elements. The elements highlighted in green have a low value of maximum principal stress, and remain intact in the concrete punching process. The boundary between yellow and green elements can be regarded as the location of cracks, as indicated by the solid lines in Fig. 13. Local stress concentrations occurred in the region where the concrete is in contact with the connector, and it did not affect the overall crack distribution. Fig. 13(b) is the sectional view of the plane where the grooves are located. The failure surface of concrete extends outward from the bottom of the groove. The embedded depth of the groove, i.e., the distance between the bottom of the groove and the outer surface of the concrete block, is defined as d. At the initiation of crack as indicated by the arrow on Fig. 13(b), the angle of failure surface is relatively small. When the failure surface extends for about 0.7d along the direction of depth, it only extends for about 0.5d along the direction of width. After that, the extension angle increases gradually. When the failure surface reaches

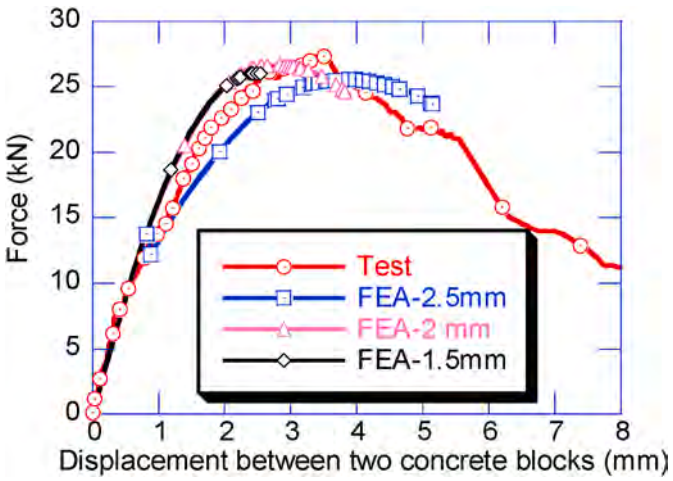

Fig. 14. Force-displacement relationships of experimental and FE analyses with different mesh sizes.

the outer surface of the concrete block, the extension width along the direction of width is about d. Fig. 13(c) is a sectional view of a plane at an angle of 45° to the plane of the groove. The ultimate extension length of the failure surface is about 1.3d. However, the angle of the initial failure surface as shown in Fig. 13(c) is smaller than that in Fig. 13(b), which indicates that less concrete participated in punching shear failure in this region of failure surface. It indicates less damage concentration in section 2-2 than in section 1-1. This phenomenon further demonstrates the assumption that the stress mainly propagated along the plane where the groove is located. Fig. 13(d) shows the stress distribution in the outer surface of the concrete block. It can be seen that the projection of the failure surface is approximately a square.

5.3. Stress analysis and failure surface identification

The development mechanism of failure surface in inner concrete was obtained in FEA. In this subsection, through a brief theoretical analysis, the method of determining the size of failure surface was proposed. Note that the concrete failure mechanism in pull-out and push-off process are similar. Therefore, the following method is applicable to concrete failure in both the pull-out and push-off process. The following description takes the pull-out condition as an example.

As demonstrated by the tests and FEA, the damage of concrete is concentrated in the plane where the groove is located. For simplicity, this plane area was isolated for analysis and the concrete in other areas is assumed as the restraint of concrete in this area. As shown in Fig. 15(a), when axial force is exerted on the connector, the load is transferred to the concrete highlighted through the contact between the groove and concrete. Internal bending stress is created in the highlighted region by the load applied. The bonding strength between FRP and concrete is ignored in this analysis since the bonding does not affect the punching failure mode. The element near the groove is subjected to normal bending stress and the shear stress caused by the external load, which can be converted into two principal stresses as shown in Fig. 15(a). In case 1, when a finite element in the highlighted region is subjected to bending tensile stress, the angle between the normal direction of equivalent principal tensile stress and vertical direction is less than 45°. In case 2, when a finite element in the highlighted region is subjected to bending compressive stress, the angle is larger than 45°. Concrete cracks when the principal tensile stress exceeds the concrete tensile strength. Therefore, the failure surface extends outward along the solid line. The projection of the solid line on the outer surface of the concrete block is almost consistent with the 45° dash line, so the failure surface along the dash line can be regarded as the equivalent failure surface, as shown in the part 1 of Fig. 15(b). The projection of failure surface along the Y-axis is illustrated at the bottom of Fig. 15(b). The width of part 1, AA', is the same as the thickness of the connector. The projected length of part 1, AB, is represented as d, which is equal to the embedded depth of the groove.

Furthermore, the punching failure surface of part 1 extends out of the X–Y plane and developed along the Z-axis within a limited range. Assume that the width of the subsequent failure surface, AC, is equal to AB, i.e., the angle between AB and BC is 45°. Thus, the failure surface of part 2 is determined. Moreover, the failure surface at the edge of the groove will extend to both sides along the Z-axis. Parallelogram BDEC is the projection of this subsequent failure surface, which is named as part 3. Three punching surfaces form a complete three–dimensional cone–like shape. The projection area of failure surface, S_a, represents the component of the failure surface in the axial direction of the connector. A geometrical formula of S_a can be described as shown in Eq. (1), where n is the number of the grooves in each connector end, d is the embedded depth of the connector groove, a is the groove width, and t is the connector thickness, as illustrated in Fig. 15(b).

$$S_a = n \times [2 \times (d \times d/2 + d \times a) + d \times t] = nd(d + 2a + t) \quad (1)$$

6. Calculation formula of axial strength

As mentioned at the beginning of section 5, the pull-out and push-off failure modes of most specimens are concrete failure (expect for the specimens that buckled under compression). After determining the failure surface of concrete and the projected failure area S_a based on the method in section 5.3, the formulas of axial strength of the connectors F_p

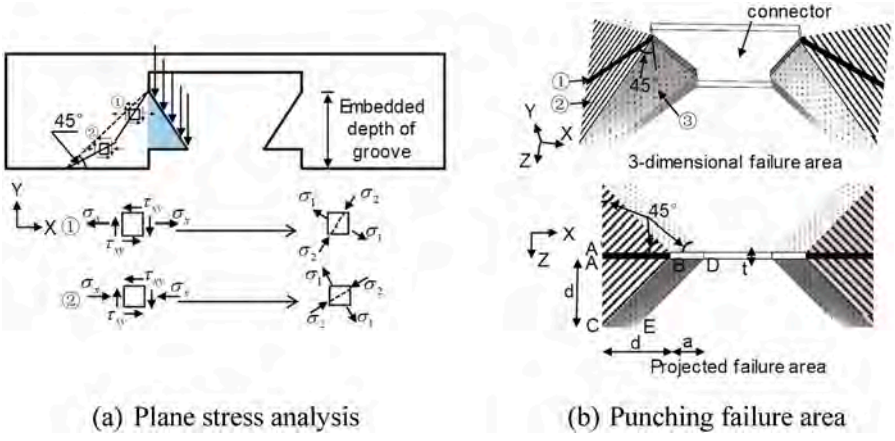

Fig. 15. Stress analysis.

can be given, as shown in Eq. (2). In this study, the tensile strength of concrete f_t is 2.19 MPa, which can be calculated according to Eq. (3) [26], where $f_{cu,k}$ is the cubic compressive strength of concrete, 34.0 MPa, determined by tests.

$$F_p = S_a f_t \tag{2}$$

$$f_t = 0.797 \times \left(0.395 \times f_{cu,k}^{0.55}\right) \tag{3}$$

Note that the axial strength formula is only applicable to the connector with concrete anchorage failure. Euler stability formula should be used in case buckling occurred.

6.1. Tensile strength

The actual failure surface in the connector pull-out process, the projected failure surface and area S_a of each connector are shown in Fig. 16. Fig. 17 compares the calculation and test results. The calculated pull-out strength of three connectors are 13.7, 14.7, and 20.6 kN, respectively, according to Eq. (2). However, the average test peak loads are 10.2, 12.1, and 15.1 kN, respectively, which are about 25% lower than the calculation results. The first reason of the discrepancy is that the formula does not consider the degree of groove anchorage effect. The small thickness of the groove and contact area can lead to unsatisfactory anchorage effect, thus affecting the size of the punching failure surface. The second reason is the imperfections of the specimens and loading equipment, resulting in the local concentration of damage on certain groove regions, and the low overall capacity. Considering the above, a correction factor β was added to the right side of Eq. (2), and the pull–out capacity formula was shown in Eq. (4). β was determined as 0.76 by ordinary least squares.

$$F_p = \beta S_a f_t \tag{4}$$

6.2. Compressive strength

In push-off tests, two typical punching failure surfaces occurred, shown in Fig. 18. Failure surface 1 is caused by the anchorage effect of the groove, which can be calculated by Eq. (1). Failure surface 2 is formed due to the pressure at the end section of the connector, which has a relatively small area. This projection area can be determined by the perimeter of the cross-section of the connector and the distance between the end section and the outer concrete surface. Both failure surfaces

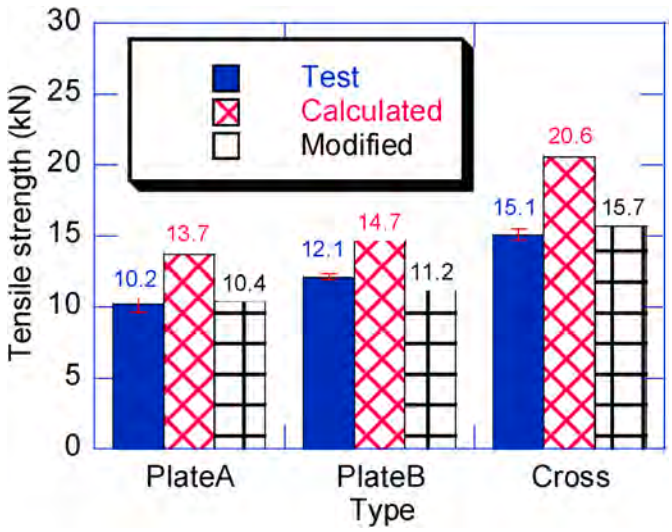

Fig. 17. Comparison between pull-out test and calculation results.

contribute to the punching capacity of the connector, but it is difficult to determine whether the two surfaces formed at the same time. Therefore, the overall punching shear capacity cannot simply be the superposition of both. The calculated value 1 and calculated value 2 in Fig. 19 are with and without consideration of the failure surface 2, representing the lower and upper bound of the punching capacity, respectively. According to Eq. (2), the values are 19.3–22.7, 20.6–25.1 and 30.2–33.7 kN, respectively, while the average punching strength of three connectors in tests are 23.9, 25.4 and 23.4 kN, respectively. It can be observed that, for the PlateA and PlateB connectors, the averages are close to the upper bound. However, the average test results of the Cross connector is much smaller than the calculation result. The possible reason is that, the small groove size, thickness and resulting small contact area with concrete leads to the potential differences in the mechanical performances of each groove. In the loading process, the stress distribution of each groove is not uniform, and the punching strength of each groove is not reached at the same time. Hence the overall punching strength of the connector is reduced.

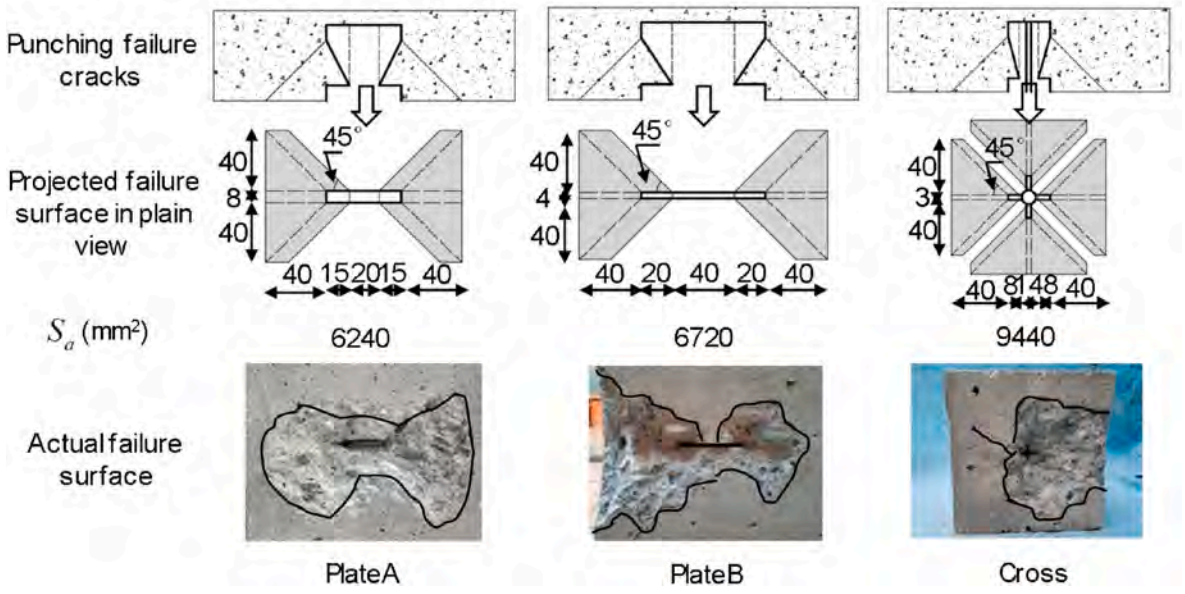

Fig. 16. Pull-out splitting failure area.

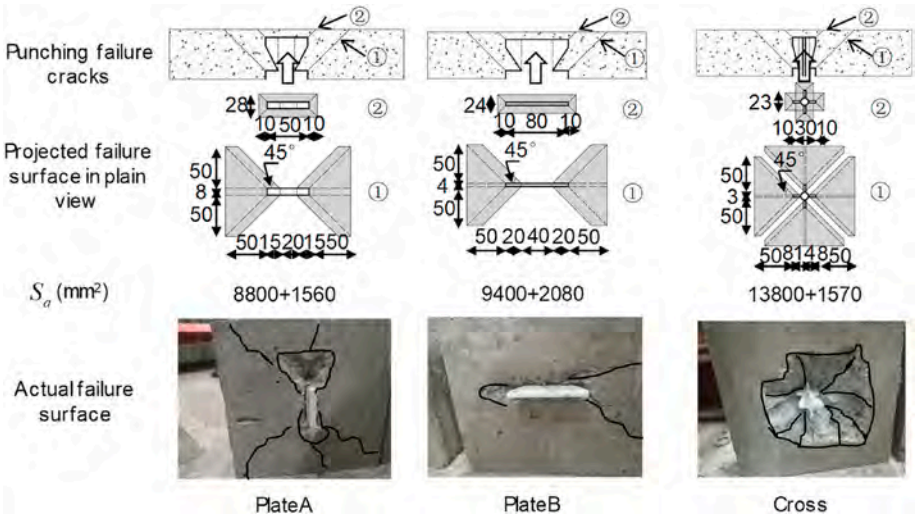

Fig. 18. Push-off punching failure area.

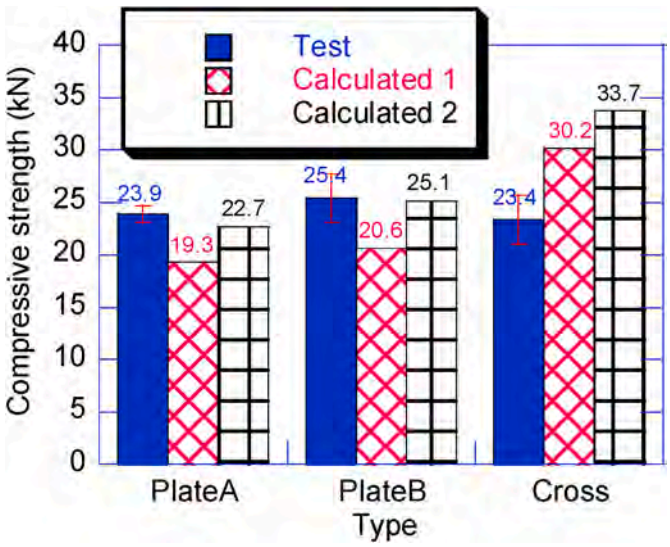

Fig. 19. Comparison between push-off test and calculation results.

7. Conclusion

This paper proposed three types of restraint connectors for SIWPs. Pull-out and push-off tests were conducted, the failure modes were investigated and the strength was obtained. Through FEA and stress analysis, method of determining the concrete failure surface was proposed, and the formulas of the axial strength was obtained, and the possible causes of errors were investigated.

Although the number of specimens is limited and the random error of the test results exists, the research is still significant. This is because the proposed method can help predict the strength of the similar connectors that adopt the "groove anchoring" method in engineering practices. In the future, more experimental data can be obtained to modify the formulas. The main conclusions of the paper are as follows:

(1) Under the pull–out action, three restraint connectors exhibited the same failure mode, i.e., anchorage zone concrete splitting and connector pull-out. Pull-out strengths of the PlateA, PlateB and Cross connectors were 10.2, 12.1 and 15.1 kN, respectively. The main factors affecting the anchorage strength were the width, height, and anchoring depth of the groove.

(2) In push-off tests, concrete punching failure was the governing failure mode of all Cross connectors with length of 60–300 mm as well as most PlateA and PlateB connectors. The 300-mm-length PlateA connector and 300&150-mm-length PlateB connectors buckled under compression. The compressive strength of PlateA, PlateB and Cross connector based on punching failure were 23.9, 25.4 and 23.4 kN, respectively.

(3) The concrete failure was mainly concentrated in the plane where the groove was located. The surrounding concrete can be considered as a constraint on the concrete in this area. The crack also expanded outward through the surrounding concrete, but the depth of the failure surface was relatively shallow.

(4) The axial strength of the connector based on concrete failure could be calculated according to the formula $F_p = \beta S_a f_t$. S_a is the projection area of failure surface, f_t is the concrete tensile strength, and β is the correction coefficient taking into account unevenness of stress distribution and the discrepancy in capacity of each groove. When β is taken as 0.76, the calculation results can be considered accurate when compared with the pull–out test results.

CRediT authorship contribution statement

Zhi-Zhou He: Conceptualization, Methodology, Test, Data process, Formal analysis, Finite element analysis, Theoretical analysis, Writing – original draft, Writing – review & editing. **Peng Pan:** Conceptualization, Methodology, Writing – review & editing. **Gen-Qi Xiao:** Methodology, Writing – review & editing, Supervision. **Shao-Dong Shen:** Writing – review & editing. **Jun-Yu Ren:** Test.

Declaration of competing interest

The authors declare that they have no known competing financial interests or personal relationships that could have appeared to influence the work reported in this paper.

Acknowledgement

The authors are grateful for financial support from the National Key R&D Program of China (Grant No. 2019YFC1509303), the Natural Science Foundation of China (Grant No. 51778342), and the Institute for Guo Qiang, Tsinghua University (Grant No. GQC0001).

References

[1] A. Einea, D.C. Salmon, G.J. Fogarasi, T.D. Culp, M.K. Tadros, State-of-the-Art of precast concrete sandwich panels, PCI J. 36 (1991) 78–98, https://doi.org/10.15554/pcij.11011991.78.98.

[2] G.T. Wade, M.L. Porter, D.R. Jacobs, Glass-Fiber Composite Connectors for Insulated Concrete Sandwich Walls, Iowa State University, 1988.

[3] J.Q. Huang, J.G. Dai, Direct shear tests of glass fiber reinforced polymer connectors for use in precast concrete sandwich panels, Compos. Struct. 207 (2019) 136–147, https://doi.org/10.1016/j.compstruct.2018.09.017.

[4] D.G. Tomlinson, N. Teixeira, A. Fam, New shear connector design for insulated concrete sandwich panels using Basalt fiber-reinforced polymer Bars, J. Compos. Construct. 20 (2016) 4016003, https://doi.org/10.1061/(ASCE)CC.1943-5614.0000662.

[5] M.L. Porter, B.R. Lehr, B.A. Barnes, Fiber Composite Connectors for Concrete Sandwich Wall Systems, Iowa State University, 1992.

[6] W.C. Xue, J.L. Yang, J.R. Wang, Pull-out tests for evaluations of anti-pulling behavior of FRP connectors in precast sandwich insulation wall panels, Fiber Reinforced Plastics/Composites 4 (2012) 56–60 (In Chinese).

[7] J. Daniel Ronald Joseph, J. Prabakar, P. Alagusundaramoorthy, Experimental studies on through-thickness shear behavior of EPS based precast concrete sandwich panels with truss shear connectors, Compos. B Eng. 166 (2019) 446–456, https://doi.org/10.1016/j.compositesb.2019.02.030.

[8] K. Hodicky, G. Sopal, S. Rizkalla, T. Hulin, H. Stang, Experimental and numerical investigation of the FRP shear mechanism for concrete sandwich panels, J. Compos. Construct. 19 (2015), 04014083, https://doi.org/10.1061/(asce)cc.1943-5614.0000554.

[9] S.H. Rizkalla, T.K. Hassan, G.W. Lucier, FRP Shear Transfer Mechanism for Precast Prestressed Concrete Sandwich Load Bearing Panels, ACI Spec. Publ., 2009, pp. 1–15.

[10] B.A. Frankl, G.W. Lucier, T.K. Hassan, S.H. Rizkalla, Behavior of precast, prestressed concrete sandwich wall panels reinforced with CFRP shear grid, PCI J. 56 (2014) 42–54, https://doi.org/10.15554/pcij.03012011.42.54.

[11] A. Chen, T.G. Norris, P.M. Hopkins, M. Yossef, Experimental investigation and finite element analysis of flexural behavior of insulated concrete sandwich panels with FRP plate shear connectors, Eng. Struct. 98 (2015) 95–108, https://doi.org/10.1016/j.engstruct.2015.04.022.

[12] H. Hou, K. Ji, W. Wang, B. Qu, M. Fang, C. Qiu, Flexural behavior of precast insulated sandwich wall panels: full-scale tests and design implications, Eng. Struct. 180 (2019) 750–761, https://doi.org/10.1016/j.engstruct.2018.11.068.

[13] X. Zhai, Y. Wang, X. Wang, Thermal performance of precast concrete sandwich walls with a novel hybrid connector, Energy Build. 166 (2018) 109–121, https://doi.org/10.1016/j.enbuild.2018.01.070.

[14] M.S.E. Imbabi, A passive–active dynamic insulation system for all climates, Int. J. Sustain. Built Environ. 1 (2012) 247–258, https://doi.org/10.1016/j.ijsbe.2013.03.002.

[15] R. O'Hegarty, O. Kinnane, Review of precast concrete sandwich panels and their innovations, Construct. Build. Mater. 233 (2020) 117145, https://doi.org/10.1016/j.conbuildmat.2019.117145.

[16] Halfen, Halfen sandwich panel anchors technical product information. https://downloads.halfen.com/catalogues/de/media/catalogues/precastsystems/SP_Leviat_19-1-E.pdf, 2016.

[17] Thermomass, Questions and answers about system NC for non-composite concrete sandwich walls. https://www.thermomass.com/website/wp-content/uploads/2017/04/thermomass_standard_systems_faq.pdf, 2017.

[18] Z. He, P. Pan, J. Ren, H. Wang, Experimental and numerical investigation of novel I-shaped GFRP connectors for insulated precast concrete sandwich wall panels, J. Compos. Construct. 24 (2020), 04020040, https://doi.org/10.1061/(asce)cc.1943-5614.0001053.

[19] He Z.Z., Pan P., Wang H.S., Design Method of Discrete Connector System for Sandwich Thermal Insulation Wall Panel. Eng. Mech. doi: 10.6052/j.issn.1000-4750.2021.03.0203 (In Chinese).

[20] ISO, Plastics Determination of Tensile Properties-Part 4: Test Conditions for Isotropic and Orthotropic Fibre-Reinforced Plastic Composites, ISO 527–4:1997, International Standards Organization, 1997.

[21] ISO, Fibre Reinforced Plastic Composites-Determination of the In-Plane Shear Stress/shear Strain Response, Including the In-Plane Shear Modulus and Strength, by the Plus or Minus 45 Degree Tension Test Method, ISO 14129-1997, International Standards Organization, 1997.

[22] ISO, Plastics-Determination of Compressive Properties, ISO 604:2002, International Standards Organization, 2002.

[23] Johnston Beer, Mechanics of Materials, second ed., McGraw Hill, 1996.

[24] ABAQUS, ABAQUS Standard User's Manual, 2010.

[25] J.S. Yuan, M.N.S. Hadi, Friction coefficient between FRP pultruded profiles and concrete, Mater. Struct. Constr. 51 (2018) 1–10, https://doi.org/10.1617/s11527-018-1250-8.

[26] Ministry of Housing and Urban-Rural Development of the People's Republic of China, Code for Design of Concrete Structures GB 50010-2010, China Architecture & Building Press, 2010.

[27] Z. Hashin, Failure criteria for unidirectional fiber composites, J. Appl. Mech. Trans. ASME. 47 (1980) 329–334, https://doi.org/10.1115/1.3153664.

[28] S.T. Pinho, P. Robinson, L. Iannucci, Fracture toughness of the tensile and compressive fibre failure modes in laminated composites, Compos. Sci. Technol. 66 (2006) 2069–2079, https://doi.org/10.1016/j.compscitech.2005.12.023.